Observational Study

Medicine

OPEN

A multiomics analysis-assisted machine learning model identifies renal hamartoma without visible fat and homogeneous clear cell renal cell carcinoma

A retrospective cohort study

Yutao Wu, MD[a], Kun Lu, MD[a], Yixiang Liao, MD[b], Jing Wang, MD[a], Tao Yang, MD[b], Li Wang, MD[b], Fei Li, MD[a,*]

Abstract

Preoperative differentiation between benign renal hamartoma without visible fat (RH-WVF) and malignant homogeneous clear cell renal cell carcinoma (hm-ccRCC) is radiologically challenging, often requiring biopsy or surgery. This study aimed to develop a noninvasive preoperative diagnostic model for distinguishing the two lesions. A retrospective analysis included 371 patients with RH-WVF or hm-ccRCC (confirmed by surgical specimens) from two Jingzhou hospitals (Jan 2015–Feb 2024). Patients were randomly divided into training (70%) and validation (30%) cohorts by tumor stage. Radiomics features were extracted from CT corticomedullary and parenchymal phases; urinary proteomic markers were also included. LASSO regression screened predictive features, and nomogram/decision tree models were built, evaluated via ROC curves and decision curve analysis. Eight radiomics and three urinary proteomic features were selected. The nomogram showed robust performance (all $P < .05$) with area under the curve (AUC) 0.889 (95% CI: 0.832–0.946) in the training cohort and 0.895 (95% CI: 0.838–0.952) in the validation cohort, outperforming the decision tree (training AUC 0.821; validation AUC 0.808). In the validation cohort, ~32% (n = 36) low-risk patients could avoid unnecessary surgery, with a 4.7% (n = 5) false negative rate. The multi-omics model integrating CT radiomics and uromics is a reliable noninvasive tool for distinguishing RH-WVF from hm-ccRCC, facilitating precise treatment and reducing unnecessary surgeries.

Abbreviations: AUC = area under the curve, C3 = complement component 3, C3AR1 = complement component 3a receptor 1, C4d = complement component 4d, C5 = complement component 5, ccRCC = clear cell renal cell carcinoma, CI = confidence interval, DICOM = Digital Imaging and Communications in Medicine, ELISA = enzyme-linked immunosorbent assay, FABP4 = fatty acid binding protein 4, FC = fold change, FN1 = fibronectin 1, hm-ccRCC = homogeneous clear cell renal cell carcinoma, HU = Hounsfield unit, ICC = intraclass correlation coefficient, IRB = Institutional Review Board, ITIH2 = inter-alpha-trypsin inhibitor heavy chain 2, LASSO = Least Absolute Shrinkage and Selection Operator, OR = odds ratio, PASEF = parallel accumulation serial fragmentation, RCC = renal cell carcinoma, RH-WVF = renal hamartoma without visible fat, ROC = receiver operating characteristic, ROI = region of interest, S100A14 = S100 calcium binding protein A14, S100A8 = S100 calcium binding protein A8, S100A9 = S100 calcium binding protein A9, VOI = volume of interest.

Keywords: clear cell renal cell carcinoma, machine learning, prediction, radiomics, renal hamartoma, uromics

1. Introduction

Renal hamartoma without visible fat (RH-WVF), as an interstitial renal tumor derived from perivascular epithelioid cells, is the most common benign renal tumor in clinical practice.[1] Approximately 5% of RH-WVF does not have enough fat to be identified through traditional imaging methods.[2,3] However, hamartomas lacking fat components or RH-WVF mainly composed of smooth muscle tissue and blood vessels with low fat are easily confused with homogeneous clear cell renal cell carcinoma (hm-ccRCC) due to their similar CT imaging characteristics to early renal cell carcinoma.[4,5] In recent years, the

YW and KL contributed equally to this study.

The authors have no funding and conflicts of interest to disclose.

The datasets generated during and/or analyzed during the current study are publicly available.

Supplemental Digital Content is available for this article.

[a] Department of Urology, The Second Hospital of Jingzhou, Jingzhou, Hubei Province, P.R. China, [b] Department of Urology, Jingzhou Hospital Affiliated to Yangtze University, Jingzhou, Hubei Province, P.R. China.

** Correspondence: Fei Li, Department of Urology, The Second Hospital of Jingzhou, Jingzhou, Hubei Province, P.R. China (e-mail: lwf0070@163.com).*

How to cite this article: Wu Y, Lu K, Liao Y, Wang J, Yang T, Wang L, Li F. A multiomics analysis-assisted machine learning model identifies renal hamartoma without visible fat and homogeneous clear cell renal cell carcinoma: A retrospective cohort study. Medicine 2025;104:52(e46862).

Received: 15 May 2025 / Received in final form: 19 November 2025 / Accepted: 20 November 2025

http://dx.doi.org/10.1097/MD.0000000000046862

incidence rate of hm-ccRCC continues to grow and maintains a high mortality rate, accounts for 2.4% of all malignancies worldwide.[6] So far, if early hm-ccRCC can be treated with timely surgical resection or chemotherapy, it can effectively control disease progression and improve prognosis.[7] However, RH-WVF and hm-ccRCC have many overlapping imaging features, especially with hm-ccRCC (considered to be hm-ccRCC without obvious necrosis, cyst, or bleeding), which often relies on biopsy or surgery for diagnosis, leading to the risk of misdiagnosis or overtreatment in RH-WVF patients.[8,9] Therefore, preoperative differentiation between benign RH-WVF and malignant hm-ccRCC remains a difficulty and challenge for surgeons in preoperative diagnosis.

In previous studies, various imaging indicators have been used as diagnostic features for RH-WVF, including plain CT density, CT histogram analysis, CT/MRI enhancement mode, chemical shift MRI parameters, T2 signal intensity ratio, and contrast-enhanced ultrasound parameters.[10,11] Most RH-WVF shows high attenuation on non-enhanced CT, low signal on T2WI MRI, uniform early enhancement and clearance patterns, which are associated with abundant blood vessels and smooth muscles.[12] However, most studies mainly focus on qualitative analysis of image features. Recently, advances in radiomics have improved the process of high-throughput extraction of quantitative statistical features, transforming image textures into exploitable data. Radiomics refers to the extraction and analysis of high-dimensional quantitative features from medical images (e.g., CT, MRI) to characterize tumor phenotypes, with applications in tumor diagnosis, prognosis, and treatment response prediction. Analyzing this data can aid in better clinical decision-making, particularly in the care of cancer patients. Fortunately, successful applications of renal tumor radiomics have been reported in predicting Fuhrman grading of renal clear cell carcinoma, distinguishing different subtypes of RCC, distinguishing RCC from benign renal tumors, and predicting survival rates of RCC patients.[13] Additionally, although imaging features can help diagnose hm-ccRCC in some aspects, they are not absolutely convincing. Nowadays, liquid biopsy technology has attracted wide attention. Urine proteomics involves the systematic analysis of proteins in urine samples to identify disease-specific biomarkers, which has shown promise in renal cancer diagnosis due to its non-invasiveness. Detection of exfoliated urinary cells has become a routine diagnostic method for bladder cancer.[14,15] It has the advantages of simple operation and high sensitivity. For hm-ccRCC, the identification of molecular markers in serum and urine can be used for screening, diagnosis and follow-up of patients. However, most studies focus on serum or urine metabolomics, microRNA, and ctDNA.

Encouraged by this, in this study, we attempted to develop and validate a multi-omics (i.e., radiomics, uroproteomics) noninvasive diagnostic prediction model that combines multi-omics labels for preoperative differentiation of RH-WVF and hm-ccRCC, in order to assist clinicians in making scientific preoperative decisions, especially for accurate evaluation of surgical indications for RH-WVF patients and hm-ccRCC.

2. Materials and methods

2.1. Study population

We conducted a retrospective search of the pathology database of The Second Hospital of Jingzhou and Jingzhou Hospital Affiliated to Yangtze University from January 2015 to February 2024 to determine patients diagnosed with RH-WVF or hm-ccRCC based on surgical resection specimens. Inclusion criteria: Patients with pathological diagnosis of RH-WVF or hm-ccRCC; The patient underwent non enhanced and contrast-enhanced CT scans less than 15 days before the surgery, and the image quality was satisfactory; and Patients with complete clinical and pathological data. Exclusion criteria: RH-WVF patients with visible lesion fat on plain CT images; Patients with hm-ccRCC have obvious necrosis, cysts, or bleeding; Patients with combined other organ functions or organic lesions; and The patient receives chemotherapy or radiation therapy before surgery. The specific process of patient inclusion and prediction model construction is summarized in Figure 1.

This study strictly followed the TRIPOD (Transparent Reporting of a multivariable prediction model for Individual Prognosis or Diagnosis) declaration and Helsinki declaration. The TRIPOD statement, published in 2015, is a widely recognized set of guidelines designed to enhance the transparency, reproducibility, and utility of multivariable prediction models, consisting of a 22-item checklist covering participant selection, predictor variables, model development, validation, and limitations. Our study adheres to its guidelines, including reporting of participant selection, predictor variables, model development, internal validation, and discussion of limitations. For ethical approval, this study was approved by the Medical Ethics Committee of The Second Hospital of Jingzhou and Jingzhou Hospital Affiliated to Yangtze University. The IRB waived the requirement for informed consent for deceased or lost-to-follow-up patients due to the retrospective nature and use of de-identified data. For living patients, written informed consent for data usage in research was obtained at the time of enrollment.

2.2. CT image acquisition and texture selection

We performed non enhanced CT scans of the renal region using ScintCare 128 slice or Hitachi LUNARIA 128 slice CT scanners. Scanning parameters: Tube voltage of 120 kV, automatic adjustment of tube current, matrix of 512 × 512, layer thickness of 5 mm, image reconstructed using multi planar reconstruction with a reconstruction layer thickness of 1 mm. The patient's CT images were imported into ITK-SNAP3.8.0 software in DICOM format, and a unified renal window was set (window width 1200 HU, window level −500 HU).

Image quality was evaluated by two radiologists (with 8 and 12 years of experience) blinded to clinical outcomes, using a 3-point scale: 1 = poor (severe motion artifacts, insufficient contrast enhancement), 2 = moderate (minor artifacts, adequate enhancement), 3 = excellent (no artifacts, optimal enhancement). Disagreements were resolved by consensus. Only images with a score ≥ 2 were included in the radiomics analysis, and the proportion of excluded images due to poor quality was 7.3%.

Two radiologists, A and B, with over 10 years of CT diagnostic experience, independently delineated the tumor region of interest (ROI) using a single blind method. Tumor ROIs were manually outlined on axial slices of contrast-enhanced CT images obtained during the venous phase, encompassing the entire solid portion of the renal mass (excluding cystic components, necrosis, or surrounding normal renal parenchyma) to generate a three-dimensional volume of interest. To evaluate the consistency of radiomics features, 30 lesions were randomly selected using the random seed method, and were r delineated by radiologist A 2 weeks later, with intraclass correlation coefficient (ICC) > 0.85 indicating good reproducibility.

In Python 3.8.1, Pyradiomics package (version 3.0) was used to extract radiomics features from ROIs, with a total of 1050 omics features extracted from each ROI. Including 14 shape features (e.g., volume, sphericity), 18 first-order features (e.g., mean, entropy), 16 gray run length matrix features, 16 gray size region band matrix features, 24 gray co-occurrence matrix features, 592 wavelet transform features, and 370 Gaussian Laplacian features.

2.3. Urine liquid chromatography tandem mass spectrometry analysis

Urine samples were collected upon admission of the patient (RH-WVF and hm-ccRCC were strictly matched with 10 cases

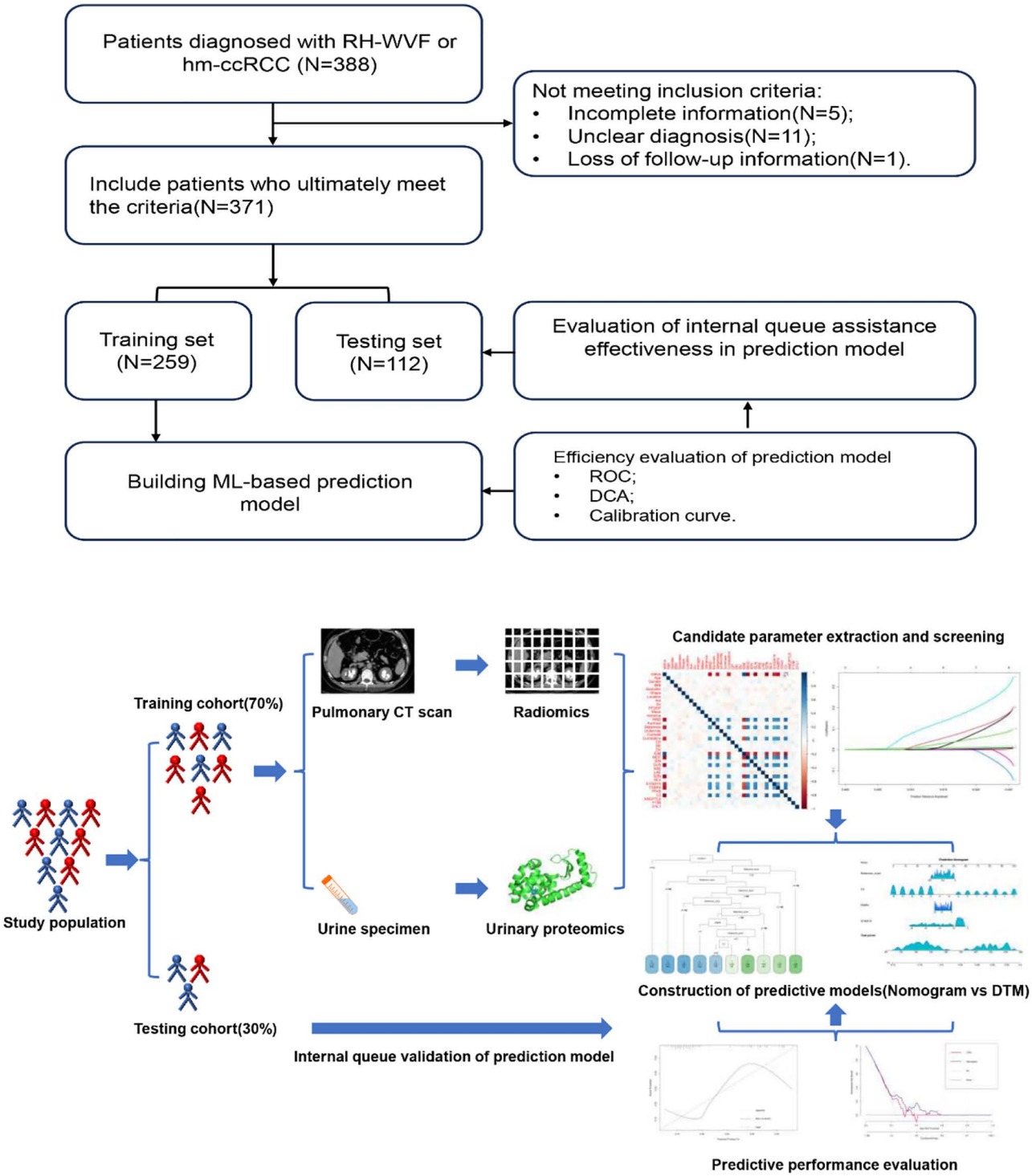

Figure 1. Flow chart for inclusion of study population and construction of prediction model.

each) as part of routine preoperative evaluation. All urine samples were calibrated at 4℃ and then centrifuged at 4000 rpm for 15 minutes at 4℃. The supernatant was collected and stored at −80℃ in our biobank until analysis. For patients admitted in 2015, urine samples were collected during initial clinical assessment and stored, with uromics analysis performed retrospectively for this study using stored samples.

After treatment with trypsin peptide solvent A/B, urine samples were analyzed by timsTOF Pro (Bruker Daltonics) mass spectrometry. The TOF detector is used to analyze precursors and fragments, with a MS/MS scanning range of 100 to 1700 m/z. TimsTOF Pro operates in parallel accumulation serial fragmentation (PASEF) mode. Select precursors with charge states ranging from 0 to 5 for fragmentation, and collect 10 PASEF-MS/MS scans per cycle. The analysis of differentially expressed proteins was performed using the "limma" package in R statistical software, where the definition of differentially expressed proteins was |log2 FC|>2 and $P < .05$. Finally, candidate protein targets in urine were determined by enzyme-linked immunosorbent assay (Table S1, Supplemental Digital Content, https://links.lww.com/MD/R51). Protein molecules with significant differences

Table 1

Patient baseline data characteristics and radiomics and urinary proteomics characteristics between RH-WVF and hm-ccRCC groups.

	Training cohort				Testing cohort			
Variables	**Overall (N = 259)**	**RH-WVF (N = 65)**	**hm-ccRCC (N = 194)**	***P* value**	**Overall (N = 259)**	**RH-WVF (N = 65)**	**hm-ccRCC (N = 194)**	***P* value**
Clinical features								
Age (median [IQR]), year	44.0 [30.0, 57.0]	45.0 [30.0, 56.0]	43.0 [29.0, 57.0]	.5	44.0 [28.0, 59.0]	44.0 [30.0, 60.0]	44.0 [28.0, 58.0]	.7
Gender (%)								
Male	105 (40.5)	30 (46.2)	75 (38.7)	.4	54 (48.2)	6 (31.6)	48 (51.6)	.2
Female	154 (59.5)	35 (53.8)	119 (61.3)		58 (51.8)	13 (68.4)	45 (48.4)	
BMI (median [IQR]), kg/m^2	24.7 [21.3, 28.4]	24.4 [22.0, 27.9]	24.9 [21.2, 28.5]	.7	24.6 [20.8, 28.3]	25.1 [21.9, 29.3]	24.5 [20.8, 27.9]	.2
Diameter (median [IQR]), mm	38.3 [21.6, 54.8]	44.1 [29.4, 62.2]	35.3 [19.6, 53.1]	.0	41.0 [26.6, 55.6]	41.5 [18.4, 55.8]	41.0 [29.6, 55.1]	.7
Shape (%)								
Round	139 (53.7)	36 (55.4)	103 (53.1)	.9	53 (47.3)	9 (47.4)	44 (47.3)	1.0
Not round	120 (46.3)	29 (44.6)	91 (46.9)		59 (52.7)	10 (52.6)	49 (52.7)	
Location (%)								
Exophytic	134 (51.7)	29 (44.6)	105 (54.1)	.2	65 (58.0)	11 (57.9)	54 (58.1)	1.0
Not exophytic	125 (48.3)	36 (55.4)	89 (45.9)		47 (42.0)	8 (42.1)	39 (41.9)	
Anl (%)								
Present	140 (54.1)	39 (60.0)	101 (52.1)	.3	55 (49.1)	7 (36.8)	48 (51.6)	.4
Absent	119 (45.9)	26 (40.0)	93 (47.9)		57 (50.9)	12 (63.2)	45 (48.4)	
Dv (%)								
Present	124 (47.9)	31 (47.7)	93 (47.9)	1.0	62 (55.4)	8 (42.1)	54 (58.1)	.3
Absent	135 (52.1)	34 (52.3)	101 (52.1)		50 (44.6)	11 (57.9)	39 (41.9)	
FFOEP (%)								
Present	138 (53.3)	30 (46.2)	108 (55.7)	.2	57 (50.9)	10 (52.6)	47 (50.5)	1.0
Absent	121 (46.7)	35 (53.8)	86 (44.3)		55 (49.1)	9 (47.4)	46 (49.5)	
First-order gray-level features								
Mean (median [IQR])	3.1 [2.3, 4.2]	3.2 [2.3, 4.1]	3.1 [2.3, 4.2]	.8	3.4 [2.3, 4.2]	3.6 [2.3, 4.6]	3.3 [2.1, 4.0]	.2
Variance (median [IQR])	5.5 [3.7, 6.9]	5.3 [4.3, 6.9]	5.5 [3.7, 7.0]	.7	5.0 [3.8, 6.7]	5.0 [3.8, 5.9]	5.1 [3.8, 6.8]	.8
MAD (median [IQR])	112.0 [87.0, 134.0]	55.0 [36.0, 68.0]	121.0 [103.0, 139.0]	<.001	114.5 [91.8, 132.3]	57.0 [45.0, 70.0]	123.0 [103.0, 136.0]	<.001
Kurtosis (median [IQR])	119.0 [61.5, 170.0]	111.0 [61.0, 167.0]	120.0 [63.0, 173.0]	.6	110.0 [60.0, 156.5]	113.0 [74.0, 151.0]	110.0 [56.0, 158.0]	.5
Skewness (median [IQR])	7.0 [3.9, 9.6]	2.5 [1.7, 3.0]	8.1 [6.2, 10.6]	<.001	7.8 [5.2, 9.8]	2.2 [1.9, 2.8]	8.5 [6.0, 10.5]	<.001
Uniformity (median [IQR])	8.8 [7.0, 11.0]	7.9 [6.8, 10.7]	9.0 [7.1, 11.2]	.0	9.0 [7.2, 10.4]	9.7 [8.8, 10.4]	8.7 [6.9, 10.4]	.2
Gray level co-occurrence matrix features								
Contrast (median [IQR])	5.4 [4.7, 6.2]	5.3 [4.7, 6.2]	5.4 [4.7, 6.2]	1.0	5.6 [4.9, 6.4]	5.4 [4.9, 5.6]	5.9 [4.9, 6.5]	.1
Correlation (median [IQR])	1.9 [1.1, 2.8]	0.6 [0.4, 0.9]	2.3 [1.7, 3.1]	<.001	2.1 [1.4, 2.7]	0.8 [0.5, 1.0]	2.4 [1.8, 2.8]	<.001
CP (median [IQR])	63.0 [36.0, 88.0]	57.0 [33.0, 88.0]	64.0 [37.0, 88.0]	.8	60.0 [32.0, 86.3]	44.0 [30.0, 63.5]	65.0 [39.0, 88.0]	.1
DE (median [IQR])	71.0 [40.0, 97.0]	70.0 [42.0, 95.0]	71.0 [39.0, 97.0]	.8	66.5 [40.0, 99.0]	49.0 [43.0, 71.5]	70.0 [40.0, 99.0]	.3
DV (median [IQR])	7.7 [5.8, 10.1]	8.1 [6.0, 10.1]	7.6 [5.8, 10.0]	.8	7.4 [5.9, 9.9]	7.2 [5.5, 10.5]	7.4 [5.9, 9.5]	.8
IDM (median [IQR])	5.0 [3.0, 7.0]	12.8 [10.2, 15.6]	3.9 [2.4, 5.4]	<.001	4.4 [2.6, 6.2]	12.3 [10.3, 14.7]	3.9 [2.5, 5.2]	<.001
MCC (median [IQR])	14.0 [9.5, 16.6]	4.7 [3.5, 6.4]	15.6 [13.2, 17.0]	<.001	13.2 [11.1, 15.7]	6.3 [4.7, 7.8]	14.0 [12.2, 16.1]	<.001
IDN (median [IQR])	48.0 [26.0, 70.0]	43.0 [19.0, 69.0]	50.0 [28.0, 72.0]	.1	46.0 [24.0, 66.8]	43.0 [23.0, 57.5]	49.0 [24.0, 69.0]	.7
Gray scale area size matrix features								
GLN (median [IQR])	80.0 [67.0, 98.0]	37.0 [25.0, 53.0]	89.0 [75.0, 102.0]	<.001	86.0 [68.0, 96.0]	31.0 [23.0, 46.0]	90.0 [77.0, 99.0]	<.001
SAE (median [IQR])	50.0 [28.5, 68.0]	47.0 [31.0, 62.0]	51.5 [27.0, 71.0]	.7	52.5 [31.0, 69.3]	38.0 [17.0, 72.5]	53.0 [34.0, 68.0]	.4
LAE (median [IQR])	114.0 [67.0, 170.0]	128.0 [90.0, 181.0]	106.0 [60.0, 167.0]	.0	106.5 [52.0, 161.3]	120.0 [62.0, 159.5]	101.0 [52.0, 161.0]	.5
SZN (median [IQR])	113.0 [93.0, 132.0]	43.0 [34.0, 67.0]	121.0 [109.0, 136.0]	<.001	117.5 [105.0, 137.0]	55.0 [32.0, 75.0]	122.0 [112.0, 141.0]	<.001
GLV (median [IQR])	45.0 [21.5, 61.5]	33.0 [18.0, 58.0]	46.0 [25.0, 62.0]	.1	33.5 [17.0, 60.0]	40.0 [24.0, 61.0]	32.0 [16.0, 58.0]	.3
Urinary proteomics								
S100A14 (median [IQR]), ng/mL	22.0 [9.5, 31.0]	6.0 [4.5, 7.0]	25.0 [19.0, 33.0]	<.001	23.0 [13.0, 31.5]	7.0 [4.5, 7.0]	26.0 [19.0, 33.0]	<.001
FABP4 (median [IQR]), ng/mL	17.0 [12.5, 22.0]	7.0 [5.0, 9.0]	17.0 [14.0, 22.0]	<.001	17.5 [13.0, 22.0]	8.0 [5.5, 9.0]	19.0 [14.0, 22.0]	<.001
C3 (median [IQR]), ng/mL	13.0 [11.0, 15.0]	5.0 [4.5, 8.0]	14.0 [13.0, 15.0]	<.001	13.0 [12.0, 15.0]	6.0 [5.5, 7.0]	14.0 [13.0, 15.0]	<.001

Anl = angular interface, BMI = body mass index, CP = cluster prominence, DE = difference entropy, DV = difference variance, Dv = dysmorphic vessels, FFOEP = fast in fast out enhancement pattern, GLN = Gray Level Non-Uniformity, GLV = Gray Level Variance, IDM = inverse difference moment, IDN = inverse difference normalized, IQR = interquartile range, LAE = large area emphasis, MAD = mean absolute deviation, MCC = maximal correlation coefficient, SAE = small area emphasis, SZN = size-zone non-uniformity.

between groups will be used for subsequent large-scale urine proteomic testing, namely S100A14 (ELISA, 96T, BJ-E3391), FABP4 (ELISA, 96T, LBK-H04227), and C3 (ELISA, 96T, ALZ228220).

2.4. Selection of candidate features and construction of predictive models

We used the Pingouin package in Python to calculate the intra observer and inter observer group correlation coefficient (ICC),

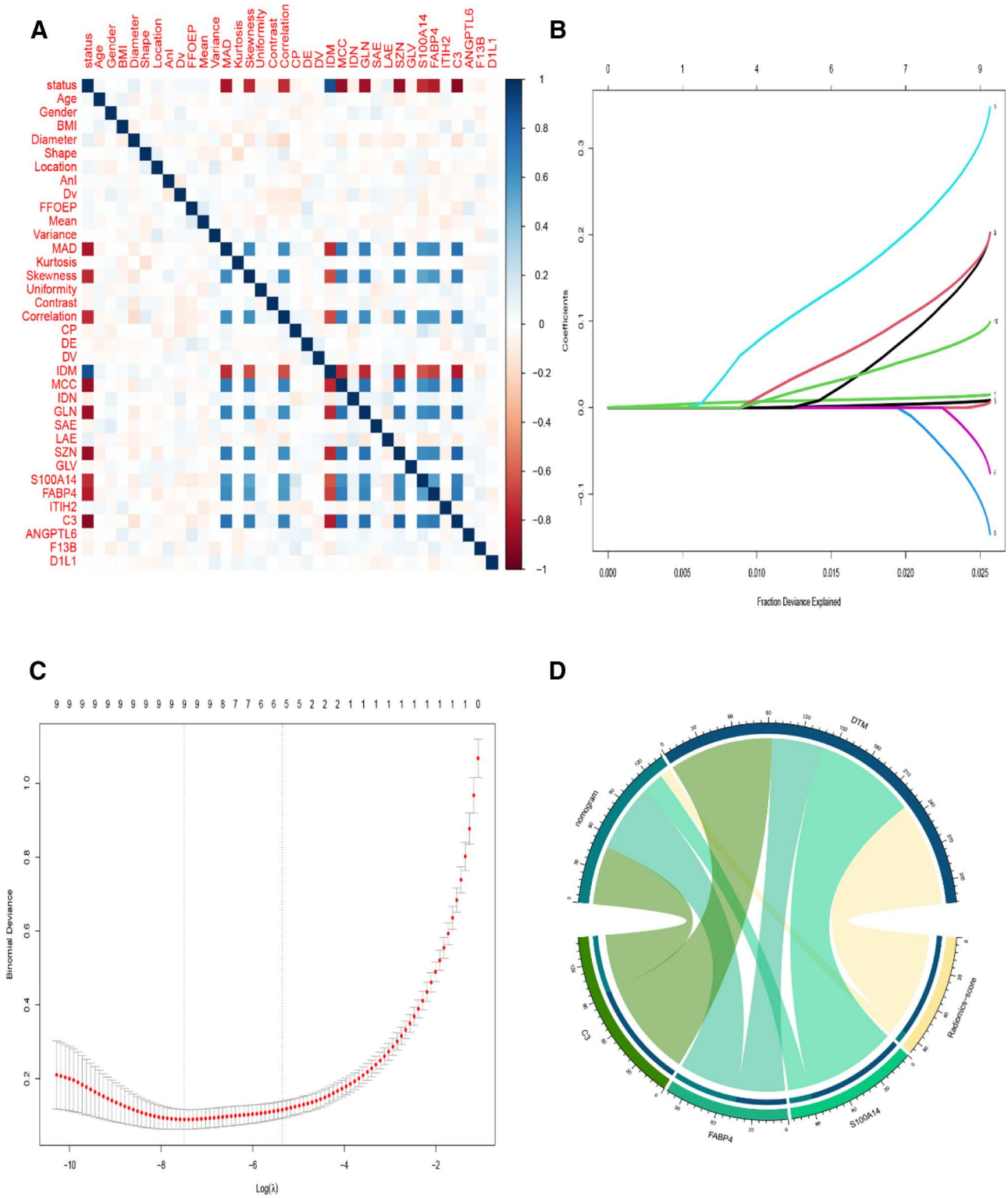

Figure 2. Selection of candidate variables. (A) Pearson correlation coefficient analysis examines the correlation between candidate variables and outcome variables. (B) Recursive selection of optimal combination candidate predictor variables based on penalty coefficient. (C) Obtain candidate variable values for inclusion in the final prediction model based on the Lambda value. (D) Weight distribution of contribution values of candidate variables in two types of prediction models.

where ICC ≥ 0.75 indicates good consistency. The cases were divided into a training set and a validation set at a 7:3 ratio via stratified random sampling. Using R software (version 4.2.1), a computer-generated random number sequence was generated, and randomization was stratified by tumor stage (I/II vs III/IV) to ensure balanced distribution of clinical characteristics between cohorts.

In the training set, *F* test and Least Absolute Shrinkage and Selection (LASSO) regression analysis with 10-fold cross-validation were used to screen for features, and the most predictive features were selected. We used univariate analysis to compare the differences in clinical factors (including clinical data, CT features, and urinary proteomics) between

Table 2

Logistic regression analysis of candidate variables for prediction model construction.

	Univariate analysis			Multivate analysis		
Variables	**OR**	**95% CI**	***P* value**	**OR**	**95%CI**	***P* value**
Radiomics score	2.26	0.99–4.56	<.05	2.29	1.01–3.99	<.05
S100A14	3.15	1.12–6.82	<.05	3.27	1.16–5.95	<.05
FABP4	1.17	0.96–2.98	<.05	1.26	1.12–3.41	<.05
C3	2.84	1.02–3.17	<.01	2.87	0.99–5.22	<.01

95% CI = 95% confidence interval, OR = odds ratio.

two groups. Variables with statistically significant differences ($P < .05$) were included in the initial model. Using significant variables from univariate analysis as inputs, a clinical factor model was constructed using multiple logistic regression analysis, and the relative risk ratio (OR) and 95% confidence interval (CI) of each independent factor were calculated to construct a nomogram.

The composite aggregate of radiomics and proteomics was constructed by first developing separate radiomics and proteomics signatures: Each signature was derived using LASSO regression, with coefficients used to weight individual features. The total score for each signature was calculated as the sum of (feature value × coefficient). The composite aggregate was then generated by combining these two signature scores using multivariable logistic regression, where the final composite score = (radiomics signature score × 0.62) + (proteomics signature score × 0.38) + 0.15, with 0.62 and 0.38 representing regression coefficients from the combined model.

In addition, we also constructed a decision tree prediction tool, incorporating radiomics and urine proteomics features with statistically significant differences into the decision tree prediction model. The Gini coefficient was used to screen and rank the features of the decision tree, and the optimal parameters of the decision tree were obtained through 10-fold cross validation of the training set.

2.5. Assessment of the performance of machine learning predictive models

The diagnostic performance of the machine learning prediction model was evaluated based on the area under the receiver operating characteristic (ROC) curve (AUC) to distinguish between RH-WVF and hm-cRCC in the training and validation sets. In addition, to evaluate the clinical effectiveness of the nomogram, decision curve analysis was performed by calculating the net benefit of a series of threshold probabilities across the entire cohort.

The DynNom tool was tested using our internal validation cohort, with performance metrics (e.g., AUC 0.87, sensitivity 89%, specificity 76%) compared to traditional diagnostic methods. High versus low risk groups were classified using the Youden index (sensitivity + specificity − 1) from the validation cohort, which identified a cutoff of 120 total points (corresponding to 65% predicted probability) as optimal.

2.6. Statistical analysis

Statistical testing and data visualization are both implemented using R statistical software (version 4.2.3, https://www.r-project.org). The clinical factor differences between the two groups were assessed using chi-square test or Fisher's exact test (categorical variables) and Mann–Whitney *U* test (continuous variables). Compare the discriminative value of each radiomics feature between RH-WVF and hm-ccRCC using one-way analysis of variance. The "glmnet" and "pROC" software packages are used to perform LASSO regression model analysis and plot ROC curves, respectively. The "rms" software package is used for the development of nomogram and the drawing of calibration curves, while Delong test is used to estimate the differences in AUC values between different models. A bilateral *P* value < .05 is considered significant.

3. Results

3.1. Baseline characteristics of patients with RH-WVF or hm-ccRCC

As shown in Table 1, a total of 371 eligible patients were screened in this study. All patients were assigned in a 7:3 ratio (training cohort: 259; validation cohort: 112) via stratified random sampling and subjected to inter-group radiomics and urinary proteomics comparisons. In the training set, we found significant inter-group differences ($P < .05$) in 7 feature parameters in radiomics, including 2 first-order features, 1 second-order feature, and 4 co-occurrence gray matrices. The same trend was also observed in the validation cohort, indicating that radiomics features have significant distinguishing characteristics between RH-WVF and hm-ccRCC. In addition, 4D label free quantitative proteomic analysis was performed on urine samples from hm-ccRCC and RH-WVF patients, revealing 113 differentially expressed proteins. Among them, 70 proteins (fold change, FC > 1.5) were identified as upregulated and 43 proteins were identified as downregulated (FC < 0.5). Figure 2A provides a heatmap of all differentially expressed genes and ultimately selects the top seven protein, namely S100A14, D1L1, FABP4, ITIH2, C3, ANGPTL6, and F13B are potential diagnostic biomarkers for RH-WVF and hm-ccRCC (Figure S1, Supplemental Digital Content, https://links.lww.com/MD/R51).

3.2. Predictive feature selection

To determine the variables most closely related to the disease (i.e. RH-WVF and hm-ccRCC), we normalized the training dataset and performed Pearson correlation coefficient heatmap analysis (Fig. 2A). Among them, disease (i.e. RH-WVF and hm-ccRCC) is used as the dependent variable, and the compressed variable coefficient is used to prevent overfitting and solve severe multicollinearity problems (Fig. 2B). The 10-fold cross validation was used to determine the optimal penalty parameter λ. We evaluated the predictive performance of the fitting model by calculating the binomial bias of the test data, choosed the latter value of λ because it leads to stricter punishment, and compared to the previous value that can further reduce the number of independent variables (Fig. 2C). Finally, as shown in Figure 2D, we developed this machine learning model using radiomics-score, S100A14, FABP4, and C3 as predictive variables.

3.3. Construction of multi-omics prediction model

As shown in Table 2, we conducted univariate and multivariate analyses to identify the risk factor associated with RH-WVF

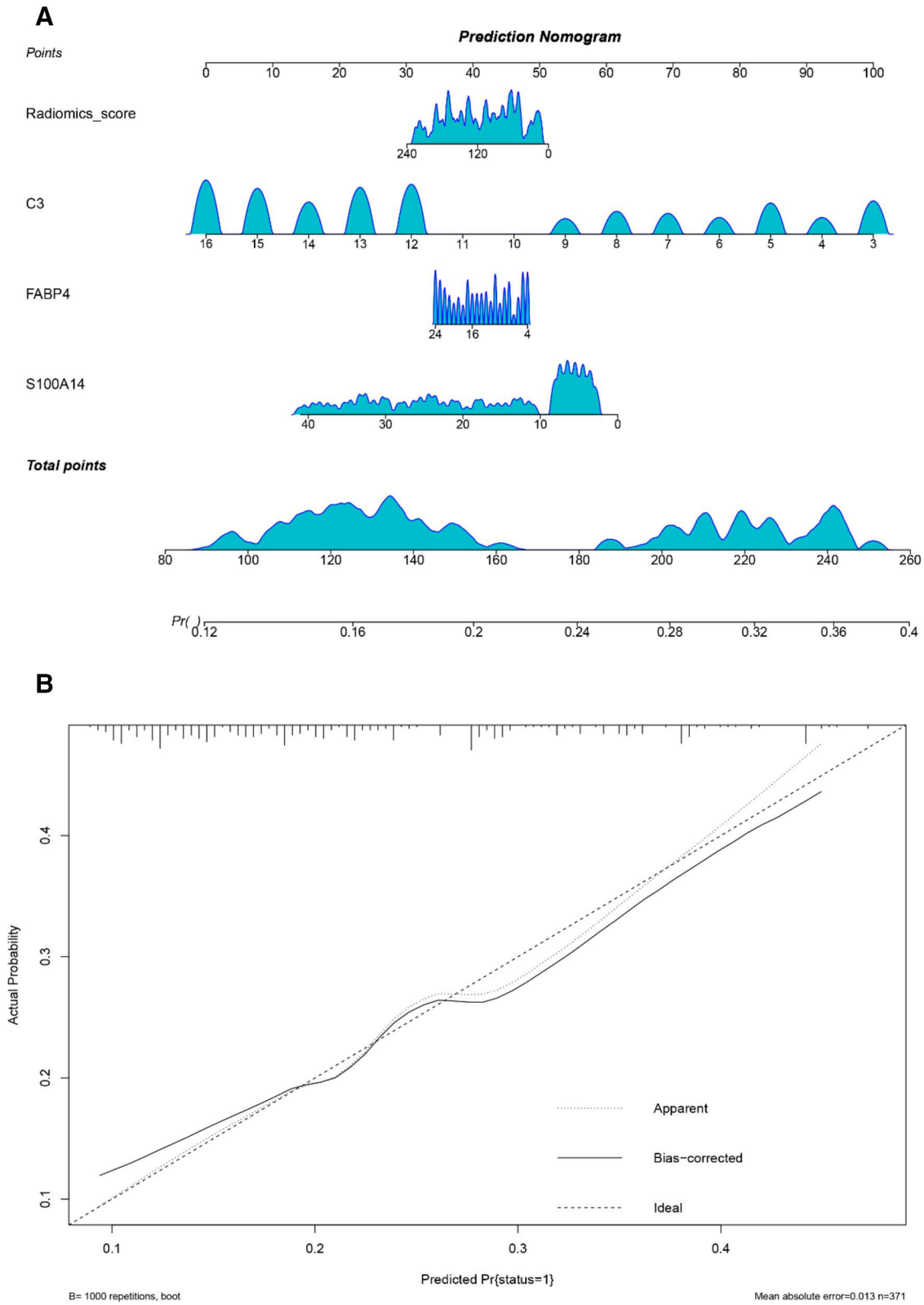

Figure 3. A visual prediction model based on nomogram. (A) Nomogram, also known as a column chart, assigns values to all variables and enables quantification. All patients use the assigned value scale and then weight it to obtain the total score, which corresponds to the predicted diagnostic value. (B) Calibration curve. During the 1000 resampling process, all variables were iteratively validated to evaluate the robustness between the predictive model and the actual values.

and hm-ccRCC. Multivariate analysis showed that radiomics-score, S100A14, FABP4, and C3 were independent predictors for distinguishing RH-WVF and hm-ccRCC. To further evaluate the results, we construct a visual prediction model based on predictive factors using the nomogram (Fig. 3A). The final nomogram is included with a key to interpretation: "To

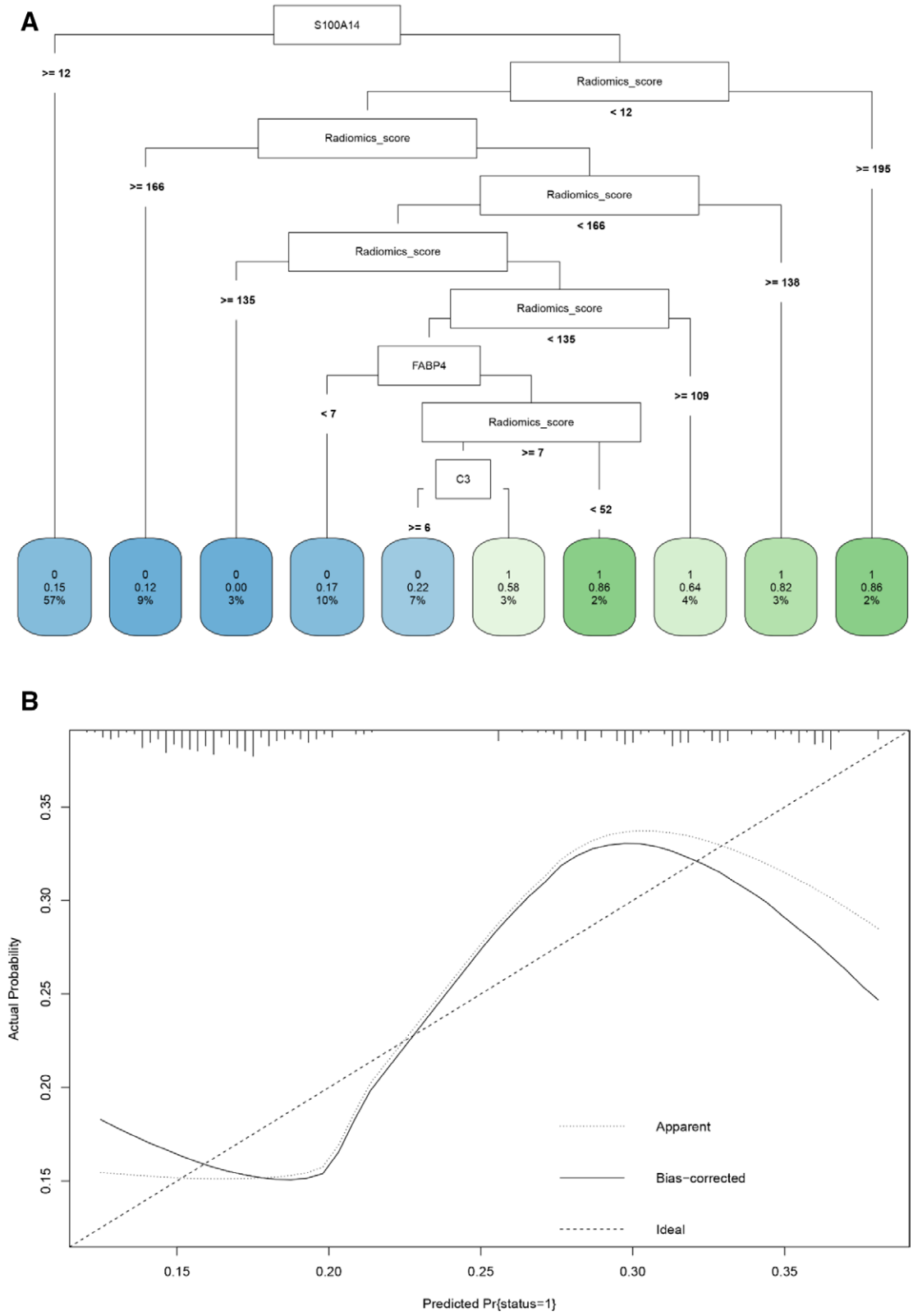

Figure 4. A discriminative prediction model based on decision tree. (A) Decision tree. All candidate variables are placed in branches of the decision tree, and discriminant analysis is performed based on thresholds. The final end of the branch is the predicted outcome. (B) Calibration curve. During the 1000 resampling process, all variables were iteratively validated to evaluate the robustness between the predictive model and the actual values.

use the nomogram: For each patient, locate their value for each variable on the corresponding axis, draw a vertical line to the 'Points' axis to determine the points for that variable, sum the points, and draw a vertical line from the 'Total Points' axis to the 'Probability of Clear Cell Renal Carcinoma' axis to obtain the predicted probability." All predictive factors are assigned numerical values, quantified in nomogram, and the total risk score is calculated.

Table 3

Diagnostic efficacy of predictive models evaluated based on receiver working characteristic curves.

	Training set				Testing set			
Prediction model	AUC	95% CI	PPV	NPV	AUC	95% CI	PPV	NPV
Nomogram	0.889	0.832–0.946	0.945	0.991	0.895	0.838–0.952	0.885	0.983
DTM	0.821	0.760–0.882	0.841	0.917	0.808	0.747–0.869	0.754	0.911

95% CI = 95% confidence interval, AUC = area under the curve, DTM = decision tree model, NPV = negative predictive value, PPV = positive predictive value.

Figure 3 was constructed using R software (version 4.2.1). Calibration curves were generated by plotting predicted probabilities against observed frequencies, with 1000 bootstrap resamples to assess calibration error. As shown in Figure 3B, we found that the C-index was as high as 0.816, indicating that the prediction model constructed based on the above prediction factors has ideal and considerable predictive performance.

Similarly, the prediction model based on decision trees, as shown in Figure 4A, selects four prediction factors (radiomics-score, S100A14, FABP4, C3) as model construction parameters after "pruning" and "iteration." Remarkably, the decision tree also showed a robust diagnostic performance with a C-index of 0.799 in distinguishing RH-WVF from hm-ccRCC (Fig. 4B).

3.4. Performance of machine learning model for distinguishing RH-WVF and hm-ccRCC

We conducted the sensitivity and specificity of the model in distinguishing RH-WVF and hm-ccRCC by comparing the area under the curve (AUC) of ROC. Correspondingly, in the training and testing cohorts, the AUC predicted by the nomogram for RH-WVF and hm-ccRCC were 0.889 (95% CI: 0.832–0.946) and 0.895 (95% CI: 0.838–0.952), respectively, with a statistically significant difference (P = .023). In contrast, the AUC values of decision trees in the training and validation sets were 0.821 (95% CI: 0.760–0.882) and 0.808 (95% CI: 0.747–0.869), respectively (Table 3). Besides, for the nomogram prediction model, the calibration curve of model performance accurately predicted the RH-WVF and hm-ccRCC (Hosmer and Lemeshow, P value = .573), the decision curve analysis results showed that the nomogram had a high net benefit for predicting RH-WVF and hm-ccRCC both in training and testing cohort (Fig. 5).

3.5. Clinical practice and efficacy evaluation of optimal prediction model

To adapt to the generalizability and universality of clinical prediction practice, we have developed an online version of prediction software based on the "DynNom" software package. As shown in Figure S2, Supplemental Digital Content, https://links.lww.com/MD/R51, we input candidate features related to patient radiomics and urine proteomics, where radiomics-score, S100A14, FABP4, C3, and risk is high; Then click on Predict to obtain the corresponding probability of predicting RH-WVF or hm-ccRCC. More importantly, the eventual prediction efficacy was significantly different between the low risk and high risk groups by the nomogram. Collectively, the nomogram based risk stratification reveals very ideal discriminative efficacy and credibility.

4. Discussion

In clinical practice, RH-WVF and hm-ccRCC represent the most common benign and malignant renal solid tumors, respectively. However, due to their shared overlapping imaging features, differential diagnosis has always been very difficult. In addition, distinguishing between RH-WVF and hm-ccRCC directly affects their prognosis, as their treatment methods are completely different, especially for hm hm-ccRCC, which does not have obvious necrosis, cysts, or bleeding. Therefore, it is urgent to seek effective diagnostic methods to reasonably and efficiently distinguish RH-WVF and hm-ccRCC before surgery. Our study indicates that a multi omics prediction model combining radiomics labels and urine proteomics has good predictive value with AUC values of 0.896 and 0.949 for distinguishing RH-WVF and hm cRCC in the training and testing sets, respectively. To our knowledge, this is the first attempt to construct a noninvasive preoperative diagnostic prediction model using radiomics and urine markers, and has achieved significant predictive results in clinical practice.

Prior to this, mounting scholars have been dedicated to building predictive tools for identifying RH-WVF and hm-ccRCC.[16] For instance, Nie et al developed a noninvasive preoperative prediction tool that combines Rad score and clinical factors, showing good predictive performance in distinguishing angiomyolipoma-wovf from hm-ccRCC.[17] Sun et al confirmed that even though there are significant differences in the performance of expert radiologists in distinguishing benign and malignant renal parenchymal masses, radiation machine learning may make up for the shortcomings.[18] In fact, inspired by this, there are many bold explorations of predictive models based on CT radiomics in the field of renal solid tumors. Especially, compared to abdominal radiologists, machine learning models trained on CT based radiological features can provide higher accuracy in distinguishing benign and malignant solid renal masses.[19] Undeniably, radiology is the process of extracting high-throughput quantitative imaging features from medical images, which represent noninvasive quantitative biomarkers that go beyond traditional imaging features visible to the human eye. In this study, unlike previous researchers, we integrated multimodal texture feature analysis, such as multi parameter extraction of first-order and second-order feature fusion co-occurrence gray matrix, which can obtain more potential highly recognized predictive biomarkers. Morever, based on the visualization mode of nomogram, multidimensional radiomics scores and urine markers can achieve a predictive efficiency of 0.895 and a C-index of 0.816, which is a very promising development prediction model in noninvasive diagnosis.

In this study, we pioneered the integration of uromics, which is not surprising as in the era of precision medicine, liquid biopsy has discovered useful biomarkers that can aid in the diagnosis and stratification of various cancers.[20] Urine, as an easily obtainable clinical sample, have been used as noninvasive, cost-effective tools for screening, diagnosis and monitoring of diseases since ancient times. So far, thousands of different proteins or peptides have been sequenced in human urine, which provides a more in-depth understanding of urine content, especially with the help of biomarkers excavated from urine samples, which has great potential in the development of noninvasive diagnosis for prostate cancer, diabetes nephropathy, chronic kidney disease and renal cell carcinoma.[21–23] As a preliminary exploration in renal solid tumors (i.e. RH-WVF

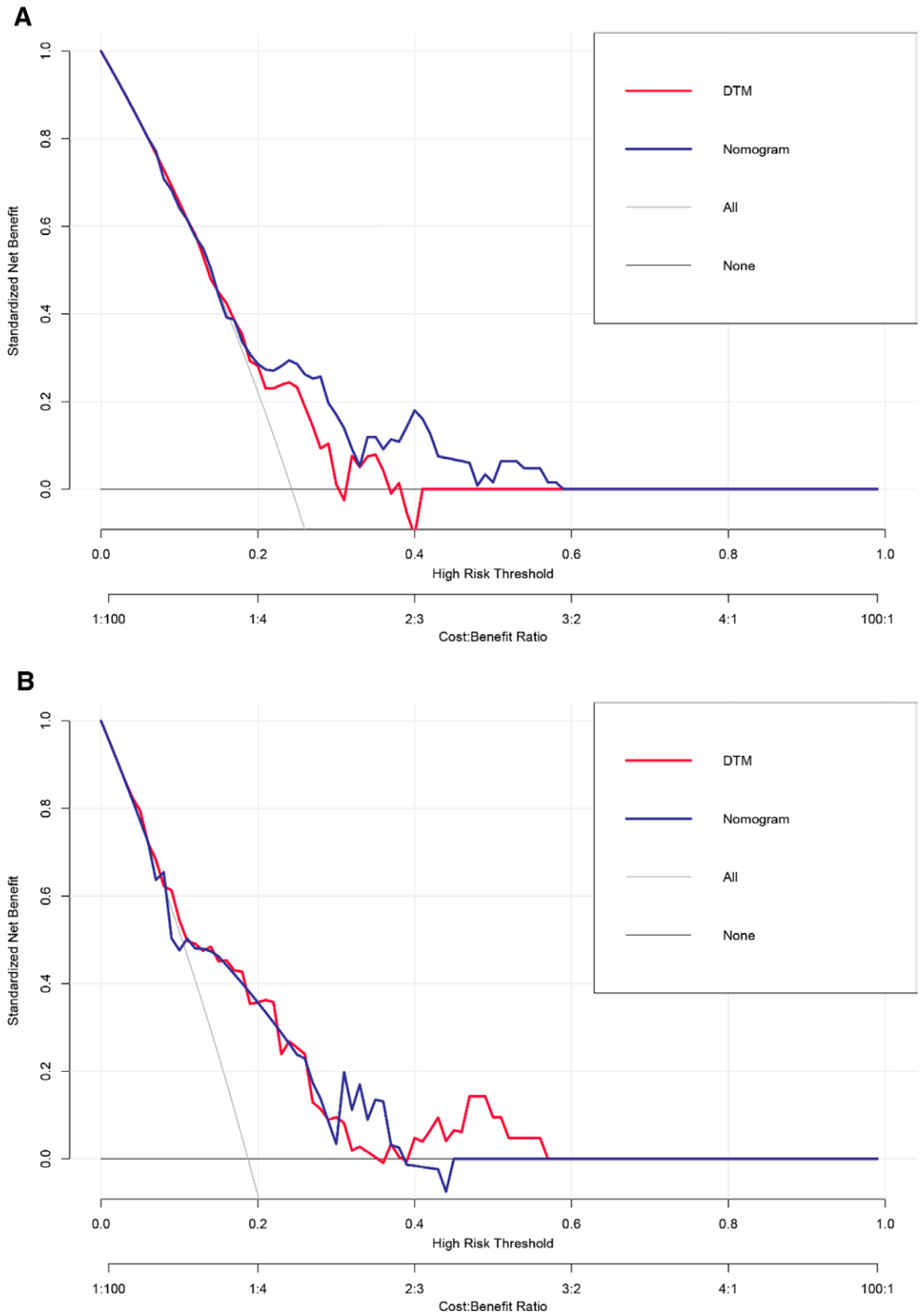

Figure 5. Performance evaluation of predictive models based on DCA. A. Training cohort; B. Testing cohort. DCA = decision curve analysis.

and hm-ccRCC), we have identified a group of highly valuable urinary proteomic markers, and the combination with radiomics has achieved extremely high predictive performance for RH-WVF and hm-ccRCC (especially hm hm-ccRCC). Beyond all doubt, the urinary protein molecules we have discovered are not novel, as in previous studies, solid evidence has precisely supported our conclusion. For example, Revel et al proposed humoral complement omics as an unbiased method for studying the overall state of the complement system in any pathological plasma sample and disease background. Its application in hm-ccRCC indicates that the elevation of C4d and Bb in plasma is a promising prognostic biomarker.[24] Indeed, the complement

system is a part of the immune system and can also affect the development of cancer. C3, C3AR1, and C5 are involved in the occurrence and development of various types of tumors.[25] Consistent with previous research findings, the biomarkers C3 could provide theoretical support for the development of a novel diagnostic tool to hm-ccRCC diagnosis.

In addition, previous studies have shown that fatty acid binding protein 4 (FABP4) has been shown to be involved in the pathogenesis of acute kidney injury induced by ischemia/reperfusion and RH-WVF abdomyolysis, and targeted inhibition of FABP4 may be a potential strategy for acute kidney injury.[26] Similarly, this study also screened FABP4 from urine proteomics and confirmed its good predictive efficacy. As a lipid-binding chaperone, FABP4 is highly expressed in adipocytes and macrophages.[27,28] We speculate that the good diagnostic efficacy of FABP4 in distinguishing RH-WVF from hm-ccRCC may be related to lipid metabolism, as FABP4 is a mandatory intermediate of macrophage endoplasmic reticulum stress response to lipids, which has been widely confirmed in the occurrence and development of malignant tumors.[29–31] Besides, Zhang et al[32] indicate that S100A8 and S100A9 may serve as biomarkers for the detection of RCC. In this study, We also found a significant difference ($P < .05$) in the urine of RH-WVF and hm-ccRCC patients with S100A14, which is highly consistent with the outcomes of previous studies. Mechanistically, S100A14 protein is an EF Ca2 + binding protein belonging to the S100 family. It is abundant in the cytoplasm of phagocytic cells and is crucial in many cellular processes, including transmitting movement and danger signals by interacting with target proteins and regulating their activity.[33,34] Collectively, these proteomic molecular markers obtained from urine demonstrate excellent predictive performance in predicting RH-WVF and hm-ccRCC. Future research combining multi omics, especially the protein molecular panel design of uromics, and the development of clinically practical test kits is imperative.

The limitations of our research are inevitably worth considering. Firstly, as a retrospective cohort study, the patients included in this study were taken from two tertiary hospitals and had a retrospective period of up to 10 years. Therefore, prospective external validation and larger sample multicenter studies are required. Secondly, the acquisition of radiomics this time mainly relies on 3-D manual ROI segmentation, which is very time-consuming and complex, especially for tumors without clear boundaries. In view of this, future research should focus on developing automatic segmentation methods for renal solid tumors with good reliability and reproducibility. Thirdly, as the first fusion analysis of radiomics and urinary proteomics, it is necessary to focus on urine multi omics (including metabolomics, transcriptomics) and integrate multiple candidate markers in the future, in order to create better diagnostic and therapeutic prediction models. We also acknowledge that real-world clinical validation is needed, and a prospective, multicenter study is planned to evaluate the DynNom tool in clinical practice.

5. Conclusion

To summarize, our research developed CT based radiomics and urine proteomics, demonstrating good predictive performance in preoperative differentiation between hm cRCC and RH-WVF. As a noninvasive and quantitative method, multi omics machine learning can be used as an effective tool to supplement conventional imaging methods for clinical decision-making processes, although further validation is needed before it can be widely applied in clinical practice.

Author contributions

Conceptualization: Yutao Wu, Fei Li.
Data curation: Fei Li.
Formal analysis: Fei Li.
Investigation: Yutao Wu, Yixiang Liao, Jing Wang, Tao Yang, Fei Li.
Methodology: Kun Lu, Tao Yang, Fei Li.
Project administration: Fei Li.
Resources: Yixiang Liao, Tao Yang, Fei Li.
Software: Yutao Wu, Kun Lu, Jing Wang, Li Wang, Fei Li.
Supervision: Fei Li.
Validation: Jing Wang, Li Wang, Fei Li.
Visualization: Kun Lu, Yixiang Liao, Jing Wang, Li Wang, Fei Li.
Writing – original draft: Yutao Wu, Fei Li.
Writing – review & editing: Fei Li.

References

[1] Flum AS, Hamoui N, Said MA, et al. Update on the diagnosis and management of renal angiomyolipoma. J Urol. 2016;195(4 Pt 1):834–46.
[2] Lim RS, Flood TA, McInnes MDF, Lavallee LT, Schieda N. Renal angiomyolipoma without visible fat: can we make the diagnosis using CT and MRI? Eur Radiol. 2018;28:542–53.
[3] Hakim SW, Schieda N, Hodgdon T, McInnes MD, Dilauro M, Flood TA. Angiomyolipoma (AML) without visible fat: ultrasound, CT and MR imaging features with pathological correlation. Eur Radiol. 2016;26:592–600.
[4] Jhaveri KS, Elmi A, Hosseini-Nik H, et al. Predictive value of chemical-shift MRI in distinguishing clear cell renal cell carcinoma from non-clear cell renal cell carcinoma and minimal-fat angiomyolipoma. AJR Am J Roentgenol. 2015;205:W79–86.
[5] Park JJ, Kim CK. Small (< 4 cm) renal tumors with predominantly low signal intensity on T2-weighted images: differentiation of minimal-fat angiomyolipoma from renal cell carcinoma. AJR Am J Roentgenol. 2017;208:124–30.
[6] Vermassen T, De Meulenaere A, Van de Walle M, Rottey S. Therapeutic approaches in clear cell and non-clear cell renal cell carcinoma. Acta Clin Belg. 2017;72:12–8.
[7] Stolpa W, Stręk-Cholewińska A, Mizia-Malarz A. clear cell renal cell carcinoma, diagnostic and therapeutic difficulties, case report and literature review. Medicina (Kaunas). 2022;58:1329.
[8] Kim TM, Ahn H, Lee HJ, et al. Differentiating renal epithelioid angiomyolipoma from clear cell carcinoma: using a radiomics model combined with CT imaging characteristics. Abdom Radiol (NY). 2022;47:2867–80.
[9] Hao YW, Zhang Y, Guo HP, et al. Differentiation between renal epithelioid angiomyolipoma and clear cell renal cell carcinoma using clear cell likelihood score. Abdom Radiol (NY). 2023;48:3714–27.
[10] Schieda N, Davenport MS, Silverman SG, et al. Multicenter evaluation of multiparametric MRI clear cell likelihood scores in solid indeterminate small renal masses. Radiology. 2022;303:590–9.
[11] Ye J, Xu Q, Wang SA, Zheng J, Zhu QQ, Dou WQ. Differentiation between fat-poor angiomyolipoma and clear cell renal cell carcinoma: qualitative and quantitative analysis using arterial spin labeling MR imaging. Abdom Radiol (NY). 2020;45:512–9.
[12] Ogawa Y, Morita S, Takagi T, et al. Early dark cortical band sign on CT for differentiating clear cell renal cell carcinoma from fat poor angiomyolipoma and detecting peritumoral pseudocapsule. Eur Radiol. 2021;31:5990–7.
[13] Mühlbauer J, Egen L, Kowalewski KF, et al. Radiomics in renal cell carcinoma-a systematic review and meta-analysis. Cancers. 2021;13:1348.
[14] Crocetto F, Barone B, Ferro M, et al. Liquid biopsy in bladder cancer: state of the art and future perspectives. Crit Rev Oncol Hematol. 2022;170:103577.
[15] Lodewijk I, Dueñas M, Rubio C, et al. Liquid biopsy biomarkers in bladder cancer: a current need for patient diagnosis and monitoring. Int J Mol Sci. 2018;19:2514.
[16] Garnier C, Ferrer L, Vargas J, et al. A CT-based clinical, radiological and radiomic machine learning model for predicting malignancy of solid renal tumors (UroCCR-75). Diagnostics (Basel). 2023;13:2548.
[17] Nie P, Yang G, Wang Z, et al. A CT-based radiomics nomogram for differentiation of renal angiomyolipoma without visible fat from homogeneous clear cell renal cell carcinoma. Eur Radiol. 2020;30:1274–84.
[18] Sun XY, Feng QX, Xu X, et al. Radiologic-radiomic machine learning models for differentiation of benign and malignant solid renal masses: comparison with expert-level radiologists. AJR Am J Roentgenol. 2020;214:W44–54.

[19] Wentland AL, Yamashita R, Kino A, et al. Differentiation of benign from malignant solid renal lesions using CT-based radiomics and machine learning: comparison with radiologist interpretation. Abdom Radiol (NY). 2023;48:642–8.
[20] Dinges SS, Hohm A, Vandergrift LA, et al. Cancer metabolomic markers in urine: evidence, techniques and recommendations. Nat Rev Urol. 2019;16:339–62.
[21] M'Koma AE, Blum DL, Norris JL, et al. Detection of pre-neoplastic and neoplastic prostate disease by MALDI profiling of urine. Biochem Biophys Res Commun. 2007;353:829–34.
[22] Gianazza E, Mainini V, Castoldi G, et al. Different expression of fibrinopeptide A and related fragments in serum of type 1 diabetic patients with nephropathy. J Proteomics. 2010;73:593–601.
[23] Molin L, Seraglia R, Lapolla A, et al. A comparison between MALDI-MS and CE-MS data for biomarker assessment in chronic kidney diseases. J Proteomics. 2012;75:5888–97.
[24] Revel M, Artero MR, Hamidi H, et al. Humoral complementomics - exploration of noninvasive complement biomarkers as predictors of renal cancer progression. Oncoimmunology. 2024;13:2328433.
[25] Dong Y, Ma WM, Yang W, et al. Identification of C3 and FN1 as potential biomarkers associated with progression and prognosis for clear cell renal cell carcinoma. BMC Cancer. 2021;21:1135.
[26] Tan Z, Guo F, Huang Z, et al. Pharmacological and genetic inhibition of fatty acid-binding protein 4 alleviated cisplatin-induced acute kidney injury. J Cell Mol Med. 2019;23:6260–70.
[27] Hotamisligil GS, Bernlohr DA. Metabolic functions of FABPs--mechanisms and therapeutic implications. Nat Rev Endocrinol. 2015;11:592–605.
[28] Furuhashi M, Hotamisligil GS. Fatty acid-binding proteins: role in metabolic diseases and potential as drug targets. Nat Rev Drug Discovery. 2008;7:489–503.
[29] Furuhashi M, Tuncman G, Görgün CZ, et al. Treatment of diabetes and atherosclerosis by inhibiting fatty-acid-binding protein aP2. Nature. 2007;447:959–65.
[30] Erbay E, Babaev VR, Mayers JR, et al. Reducing endoplasmic reticulum stress through a macrophage lipid chaperone alleviates atherosclerosis. Nat Med. 2009;15:1383–91.
[31] Tsujimoto M, Aoki K, Ohnishi A, Goto Y. Endoplasmic reticulum aminopeptidase 1 beyond antigenic peptide-processing enzyme in the endoplasmic reticulum. Biol Pharm Bull. 2020;43:207–14.
[32] Zhang L, Jiang H, Xu G, et al. Proteins S100A8 and S100A9 are potential biomarkers for renal cell carcinoma in the early stages: results from a proteomic study integrated with bioinformatics analysis. Mol Med Rep. 2015;11:4093–100.
[33] Donato R. S100: a multigenic family of calcium-modulated proteins of the EF-hand type with intracellular and extracellular functional roles. Int J Biochem Cell Biol. 2001;33:637–68.
[34] Donato R. Functional roles of S100 proteins, calcium-binding proteins of the EF-hand type. Biochim Biophys Acta. 1999;1450:191–231.